



Radial gravity currents in vertically graded porous media: Theory and experiments for Newtonian and power-law fluids



Vittorio Di Federico^a, Sandro Longo^{b,*}, Luca Chiapponi^b, Renata Archetti^a, Valentina Ciriello^a

^a Dipartimento di Ingegneria Civile, Chimica, Ambientale e dei Materiali (DICAM), Università di Bologna, Viale Risorgimento, 2, 40136 Bologna, Italy

^b Dipartimento di Ingegneria Civile, Ambiente Territorio e Architettura (DICAteA), Università di Parma, Parco Area delle Scienze, 181/A, 43124 Parma, Italy

ARTICLE INFO

Article history:

Received 22 December 2013

Received in revised form 17 April 2014

Accepted 21 April 2014

Available online 30 April 2014

Keywords:

Porous

Gravity current

Similarity solution

Variable permeability

Non-Newtonian

Laboratory experiments

ABSTRACT

This study theoretically and experimentally explores the behaviour of axisymmetric gravity currents of Newtonian and power-law fluids in inhomogeneous porous media. Systematic heterogeneity along the vertical is represented by a power-law permeability variation governed by the parameter ω , mimicking trends in natural media. A self-similar solution describing (i) the rate of propagation and (ii) the profile of the current is derived by considering a current of volume proportional to time raised to a non-negative power α . Four critical values of α are determined: the first two affect the time dependency of the radius, height and average gradient of the current on flow behaviour index n and ω ; the third one dictates if the current accelerates or decelerates; the fourth one governs the asymptotic validity of the thin current approximation. Experimental validation is performed using shear-thinning suspensions and Newtonian mixtures in constant- and variable-flux regimes. A stratified porous medium composed of four uniform strata of glass beads with different diameters is used for this purpose. The experimental results for the radius and profile of the current agree well with the self-similar solution except at the beginning of the process, due to the limitations of the 1-D assumption and to boundary effects near the injection zone. An uncertainty analysis indicates that the rheological fluid behaviour and the variation in permeability significantly affect the propagation of the current.

© 2014 Elsevier Ltd. All rights reserved.

1. Introduction

Extensive research has been conducted on gravity-driven motion through porous media. These studies have been motivated by several geophysical and industrial applications, including enhanced oil recovery, contaminant migration, seawater intrusion, and carbon dioxide sequestration in geological formations [1–4]. The behaviour of porous gravity currents is generally analyzed by considering the release of a time-variable volume of an intruding fluid in an infinite domain under the thin current assumption. Solutions in self-similar form were derived by Huppert and Woods [5] for plane geometry and by Lyle et al. [6] for axisymmetric geometry. Di Federico et al. [7,8] recently extended these studies to non-Newtonian flow, to handle the complex rheological nature of many fluids involved in relevant applications. These include injection of displacing suspensions or muds in enhanced oil recovery and well drilling [9,10], crude oil flow in reservoirs [11], soil remediation via nanoparticles advected by fluid carriers [12], subsurface contamination by polymeric pollutants (e.g. [13] and

references therein), soil grouting [14], flow of blood in biological porous media [15], blood filtration through reticulated foams [16]. Diverse rheological models are available in the literature for the description of non-Newtonian behaviour [17]; among these, the simplest is represented by the two-parameter power-law model. This formulation usually provides an accurate approximation in the intermediate shear rate range, as demonstrated in e.g. Longo et al. [18], where a power-law model satisfactorily fitted rheometric measurements of shear-thinning fluids in the interval $0.1\text{--}5\text{ s}^{-1}$.

In addition to rheological fluid behaviour, the propagation of gravity driven flow in natural porous formations is strongly affected by heterogeneity [19]. Vertical permeability and porosity gradients have been shown to condition front propagation in plane fluid drainage from an edge [20]. In a two-layered porous medium and above a critical influx, the intruding fluid overrides the low-permeability lower layer, enhancing mixing [4]. Investigation into the combined effects of fluid rheology and spatial permeability variations is crucial in several applications in natural porous media (e.g. [21]). The present study focuses on systematic permeability variations of the kind extensively adopted in the porous media literature [2,20,22–24]; these closed-form expressions approximately

* Corresponding author. Tel.: +39 0521 90 5157; fax: +39 0521 90 5924.

E-mail address: sandro.longo@unipr.it (S. Longo).

mimic trends occurring in natural media. A coupled theoretical and experimental approach is used here to analyse the influence of vertical permeability gradients perpendicular to the flow direction on axisymmetric non-Newtonian power-law gravity currents with time-variable inflow. First, the problem is formulated in dimensionless form (Section 2.1) and a similarity solution that generalises the results of Di Federico et al. [8] is derived (Section 2.2). Second, the dependency of the radius and height of the current on problem parameters is discussed (Section 3). The theoretical solution was tested against data from laboratory experiments conducted with shear-thinning suspensions and Newtonian mixtures in constant- and variable-flux regimes; the experimental setup is described in Section 4.1, while the results of the experiments are presented and compared with the theory in Section 4.2. The goodness of the approximation provided by the proposed formulation is examined via an ad hoc uncertainty analysis (Section 4.3). A set of conclusions closes the paper (Section 5).

2. Theoretical model

2.1. Formulation

Consider the setting depicted in Fig. 1, in which r and z represent radial and vertical coordinates respectively. An axisymmetric gravity current of a non-Newtonian fluid of uniform density ρ , with rheology described by a power-law model $\tau = m|\dot{\gamma}|^{n-1}\dot{\gamma}$, with τ and $\dot{\gamma}$ the shear stress and rate, m the consistency index, and n the flow behaviour index, is released at the origin and intrudes into an infinite porous domain of depth h_0 saturated with another fluid of uniform density $\rho - \Delta\rho$. The intruding current, described by its height $h(r, t)$ in the sharp interface approximation, extends above a horizontal impermeable bed to a coordinate denoted by $r_N(t)$. We consider the case of a isotropic heterogeneous domain in which the medium permeability k (dimensions $[L^2]$) is constant in the horizontal direction but has a vertical gradient described by [2]

$$k(z) = k_0(z/r^*)^{\omega-1}, \quad (1)$$

where k_0 is a characteristic permeability, r^* is a length scale, and ω is a constant. Values of $\omega < 1$, $\omega = 1$ and $\omega > 1$ represent negative, null, and positive gradients with elevation, respectively. A lower bound is set to the value of ω for assigned n , i.e. $\omega > \omega_0 = (n-1)/(n+1)$. This ensures the validity of the self-similar solutions derived in the sequel; physically, it is equivalent to limit the permeability decrease with elevation. For a Newtonian fluid ($n = 1$), $\omega_0 = 0$, as earlier noted by Ciriello et al. [2] and

Mathunjwa and Hogg [25]. Note that the permeability tends to decrease with depth in natural porous and fractured media [22,23], rendering the case $\omega \geq 1$ decidedly more common than $\omega < 1$. We also assume that capillary effects are negligible and that the thin current approximation holds, which allows us to disregard motion in the ambient fluid and vertical velocities in the intruding fluid. Under these assumptions, the pressure distribution in the intruding current is hydrostatic and given, for $0 \leq z \leq h$, by $p(r, z, t) = p_1 + \Delta\rho gh(r, t) - \rho gz$, where $p_1 = p_0 + (\rho - \Delta\rho)gh_0$ is a constant and p_0 is the constant pressure at $z = h_0$.

The equation of motion of a non-Newtonian power-law fluid in a porous medium is given by [26,27]

$$\nabla p - \rho \mathbf{g} = -\frac{\mu_{\text{eff}}}{k} |\mathbf{u}|^{n-1} \mathbf{u} \quad (2)$$

where p is the pressure, \mathbf{u} the Darcy velocity, \mathbf{g} the acceleration due to gravity, and μ_{eff} the effective viscosity (dimensions $[M L^{-n} T^{n-2}]$). The inverse of the proportionality factor that appears in (2) is termed ‘mobility’ and is expressed as [8]

$$\frac{k}{\mu_{\text{eff}}} = \frac{1}{2C_t} \frac{1}{m} \left(\frac{n\phi}{3n+1} \right)^n \left(\frac{50k}{3\phi} \right)^{(n+1)/2}, \quad (3)$$

where ϕ and $C_t (> 1)$ represent medium porosity and tortuosity, respectively. The latter factor empirically accounts for the complex nature of non-Newtonian fluid flow in porous media. As such, it has been expressed in several ways in the literature in the form $C_t = C_t(n)$ [28], with the various formulations differing significantly. The expression proposed by Pascal [29], i.e., $C_t = (25/12)^{(n+1)/2}$ simplifies the mobility expression to $k/\mu_{\text{eff}} = (1/(2m)) (n\phi/(3n+1))^n (8k/\phi)^{(n+1)/2}$ and, for a Newtonian fluid ($n = 1$), allows (2), combined with (3), to reduce to Darcy’s law, $\nabla p - \rho \mathbf{g} = -(\mu/k)\mathbf{u}$, where μ is the dynamic viscosity. Pascal’s formulation for the tortuosity is adopted in the interpretation of the experimental results. The hydrostatic assumption allows the pressure gradient to be expressed as a function of the unknown free surface as $\partial p/\partial r = \Delta\rho g(\partial h/\partial r)$, which, together with (1) and (2), yields the following expression for Darcy velocity in the r direction for purely horizontal flow:

$$u(r, z, t) = -(\Delta\rho g)^{1/n} k_0^{(n+1)/(2n)} \left(\frac{z}{r^*} \right)^{\frac{(\omega-1)(n+1)}{2n}} \left| \frac{\partial h}{\partial r} \right|^{1/n-1} \frac{\partial h}{\partial r}, \quad (4)$$

$$A = A(\phi, m, n) = \frac{1}{2C_t} \left(\frac{50}{3} \right)^{(n+1)/2} \left(\frac{n}{3n+1} \right)^n \frac{\phi^{(n-1)/2}}{m}, \quad (5)$$

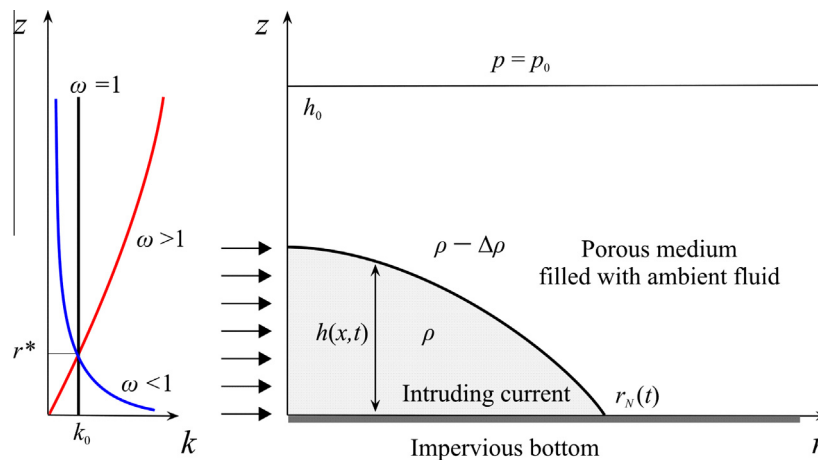


Fig. 1. Sketch of an axisymmetric gravity current intruding into a saturated porous medium of thickness h_0 . The left panel illustrates vertically increasing ($\omega > 1$), decreasing ($\omega < 1$) and homogeneous ($\omega = 1$) permeabilities.

where the latter factor reduces to $A = 1/\mu$ for a Newtonian fluid ($n = 1$). For $\omega < 1$, the behaviour of (4) is singular for $z \rightarrow 0$, but this does not affect the overall behaviour of the current. The local continuity condition takes the following form [6]

$$\frac{1}{r} \frac{\partial}{\partial r} \left(r \int_0^h u dz \right) = -\phi \frac{\partial h}{\partial t}. \quad (6)$$

The global mass balance equation for a variable-volume inflow is as follows:

$$2\pi\phi \int_0^{r_N(t)} rh(r, t) dr = Qt^\alpha, \quad (7)$$

where Q (dimensions $[L^3 T^{-\alpha}]$) and α are constants. For an instantaneous fluid release ($\alpha = 0$), Q is the volume of the current; for a continuous injection ($\alpha > 0$), the volumetric discharge is $Q' = \alpha Qt^{\alpha-1}$. For high values of the Bond number (the influence of surface tension effects is limited), the problem statement is completed by the boundary condition at the current front

$$h(r_N(t), t) = 0. \quad (8)$$

The previous equations may be non-dimensionalised by setting $T = t/t^*$, $R = r/r^*$, $R_N = r_N/r^*$, and $H = h/r^*$, where, for $\alpha \neq 3$, the time, space, and velocity scales are

$$t^* = \left(\frac{Q}{\phi v^*} \right)^{1/(3-\alpha)}, \quad r^* = v^* t^*, \quad v^* = \frac{(\Delta\rho g)^{1/n} k_0^{(1+n)/(2n)}}{\phi}. \quad (9)$$

The special case of $\alpha = 3$ requires a different non-dimensional formulation since the proposed time scale breaks down and an additional velocity scale arises [7,30], as addressed in Appendix A. The scaled equation satisfied by the interface profile for $\alpha \neq 3$, obtained by combining the dimensionless versions of (4) and (6), is as follows

$$\frac{1}{F_1} \frac{1}{R} \frac{\partial}{\partial R} \left[RH^{F_1} \left| \frac{\partial H}{\partial R} \right|^{1/n-1} \frac{\partial H}{\partial R} \right] = \frac{\partial H}{\partial T}, \quad (10)$$

$$F_1 = \frac{(\omega - 1)(n + 1) + 2n}{2n}, \quad (11)$$

where the factor F_1 reduces to unity for a homogeneous aquifer. The dimensionless form of (7) is

$$2\pi \int_0^{R_N} RH dR = T^\alpha. \quad (12)$$

Finally, boundary condition (8) is unchanged in dimensionless coordinates.

2.2. Self-similar solution

Eqs. (10) and (12) provide scaling relationships for the current length R and height H with time given by $R \sim T^{F_2}$ and $H \sim T^{F_3}$, with

$$F_2 = \frac{[(\omega - 1)(n + 1) + 2]\alpha + 2n}{2[(\omega(n + 1) + 2)]}, \quad F_3 = \frac{(n + 1)\alpha - 2n}{\omega(n + 1) + 2}. \quad (13)$$

Hence a convenient similarity variable to solve the system of governing equations takes the form

$$\eta = F_1^{F_4} R/T^{F_2}, \quad F_4 = \frac{n}{\omega(n + 1) + 2} \quad (14)$$

with a prefactor defined to simplify subsequent expressions. The system permits self-similar solutions for front position and current height of the form $R_N(T) = (\eta_N/F_1^{F_4})T^{F_2}$ and $H(R, T) = F_1^{F_4} T^{F_3} f(\eta)$, where η_N is defined as the value of η at the current nose $R = R_N(T)$. Introducing a normalised similarity variable $\zeta = \eta/\eta_N$, $f(\eta)$ is rescaled as $f(\eta) = \eta_N^{F_5} \psi(\zeta)$, where

$$F_5 = \frac{2(n + 1)}{(\omega - 1)(n + 1) + 2} \quad (15)$$

and the final form for the dimensionless current profile becomes

$$H(R, T) = F_1^{2F_4} \eta_N^{F_5} T^{F_3} \psi(\zeta), \quad (16)$$

in which ψ is the thickness profile. Adoption of (14) through (16) yields the following expressions for (10) and (12) respectively:

$$\left(\zeta \psi^{F_1} \psi' |\psi'|^{1/n-1} \right)' + F_2 \zeta^2 \psi' - F_3 \zeta \psi = 0, \quad (17)$$

$$\eta_N = \left(2\pi \int_0^1 \zeta \psi(\zeta) d\zeta \right)^{-1/(F_5+2)} \quad (18)$$

with

$$\psi(1) = 0, \quad (19)$$

where the prime indicates $d/d\zeta$. For $\omega = 1$, the governing equations and results reduce to those derived by Di Federico et al. [8] for non-Newtonian gravity currents in homogeneous porous media. The numerical factors defined earlier become $F_1 = 1$, $F_2 = (\alpha + n)/(n + 3)$, $F_3 = [\alpha(n + 1) - 2n]/(n + 3)$, $F_4 = n/(n + 3)$, and $F_5 = n + 1$. For $n = 1$ and any ω , results can be derived for Newtonian axisymmetric gravity currents flowing in vertically graded media; in this case, $F_1 = \omega$, $F_2 = (\alpha\omega + 1)/[2(\omega + 1)]$, $F_3 = (\alpha - 1)/(\omega + 1)$, $F_4 = 1/[2(\omega + 1)]$, and $F_5 = 2/\omega$. For $n = 1$ and $\omega = 1$, the previous expressions can be further simplified to those derived by Lyle et al. [6] in dimensional form, and $F_1 = 1$, $F_2 = (\alpha + 1)/4$, $F_3 = (\alpha - 1)/2$, $F_4 = 1/4$, and $F_5 = 2$. The general equations can be solved analytically for a current of constant volume ($\alpha = 0$), yielding the following solutions:

$$\psi(\zeta) = \left[\frac{(\omega - 1)(n + 1) + 2}{2(n + 1)} \left(\frac{n}{\omega(n + 1) + 2} \right)^n (1 - \zeta^{n+1}) \right]^{\frac{2}{(\omega-1)(n+1)+2}}, \quad (20)$$

$$\eta_N = \left[\frac{2(n + 1)}{(\omega - 1)(n + 1) + 2} \left(\frac{\omega(n + 1) + 2}{n} \right)^n \right]^{\frac{1}{\omega(n+1)+2}} \times \left[\frac{\omega(n + 1) + 2}{2\pi} \frac{\Gamma\left(\frac{2}{n+1}, \frac{\omega(n+1)+2}{(\omega-1)(n+1)+2}\right)}{\Gamma\left(\frac{2}{n+1}\right)\Gamma\left(\frac{2}{(\omega-1)(n+1)+2}\right)} \right]^{\frac{(\omega-1)(n+1)+2}{2(\omega(n+1)+2)}}, \quad (21)$$

where $\Gamma(\cdot)$ is the gamma function. The latter solution is consistent with the limitation $\omega > (n - 1)/(n + 1)$ introduced in the problem setup. For $\omega = 1$, (20) and (21) reduce to Eq. (17) in [8]. For $n = 1$ and any $\omega > 0$, (20) and (21) become

$$\psi(\zeta) = \left[\frac{\omega}{4(\omega + 1)} (1 - \zeta^2) \right]^{1/\omega}, \quad (22)$$

$$\eta_N = \left[\frac{4(\omega + 1)}{\omega} \right]^{1/[2(\omega+1)]} \left(\frac{\omega + 1}{\pi\omega} \right)^{\omega/[2(\omega+1)]}. \quad (23)$$

For $n = 1$ and $\omega = 1$, the classical result obtained by Pattle [31], $\psi(\zeta) = (1 - \zeta^2)/8$ and $\eta_N = 2/\pi^{1/4}$, is recovered. To numerically integrate (17) a second boundary condition is obtained in addition to (19) by: (i) generating an asymptotic solution near $\zeta = 1$ in terms of a power (Frobenius) series; (ii) deriving it to obtain a condition on the first derivative of ψ as

$$\psi'|_{\zeta=1} = -a_0 b \epsilon^{b-1}, \quad a_0 = \left(\frac{b^{1/n}}{F_2} \right)^{-nb}, \quad b = \frac{1}{1 + n(F_1 - 1)}, \quad (24)$$

where $\epsilon = 1 - \zeta$ is a small quantity, and b is non negative due to the constraint $\omega > (n - 1)/(n + 1)$.

It is worth noticing that the differential Eq. (17) becomes singular both in the origin ($\zeta = 0$), because of the vanishing of the higher order term, and at the front ($\zeta = 1$), due to boundary condition (8). Near the origin, the self-similar solution for $\alpha \neq 0$ is inconsistent with model assumptions, as the small-slope approximation is violated. As suggested by Di Federico et al. [8], one can exclude from the numerical computation a small cylinder containing a volume of fluid negligible with respect to the injected volume (except possibly for $T \rightarrow 0$). This does not influence the numerical solution, which is obtained integrating from the front end of the current. The singularity near the current tip is treated approximating the solution with a Frobenius series. For $\epsilon \neq 0$, $\psi'(1 - \epsilon)$ is always negative and finite, and the boundary condition near the front end is a continuous function of ω .

3. Discussion of results

The time exponents F_2 and F_3 of the radius and height of the gravity current are given by (13) and depend on the time rate of change of the fluid volume, α , the flow behaviour index n , and the permeability variation along the vertical, parametrized by ω .

Both F_2 and F_3 are increasing functions of α under model assumptions; F_3 is so for any ω , while F_2 increases with α for $\omega > \omega_0 = (n - 1)/(n + 1)$. The dependence of F_2 and F_3 on n and ω is more complex. It is found that for a first critical value $\alpha_\omega = 2n/(n + 1)$, F_2 and F_3 are independent on the permeability variation ω and take the values $F_2(\alpha_\omega) = n/(n + 1)$ and $F_3(\alpha_\omega) = 0$. For $\alpha < \alpha_\omega$, F_2 is a decreasing function of ω ; the reverse is true for $\alpha > \alpha_\omega$. The behaviour of F_3 is opposite to that of F_2 , as it increases/decreases with ω for $\alpha < \alpha_\omega$ or $\alpha > \alpha_\omega$. For a second critical value $\alpha_n = \omega + 2$, F_2 and F_3 are independent on the flow behaviour index n , reducing to $F_2(\alpha_n) = (\omega + 1)/2$ and $F_3(\alpha_n) = 1$. For $\alpha < \alpha_n$, F_2 is an increasing function of n ; the reverse is true for $\alpha > \alpha_n$. Again, the behaviour of F_3 is opposite to that of

F_2 , as the radius and the average height of the current are inversely proportional by virtue of mass balance.

To provide a physical explanation of the observed tendencies, it is useful to evaluate the average free-surface gradient driving the motion, given by

$$\left(\frac{\partial H}{\partial R}\right) = F_1^{3F_4} \eta_N^{F_5-1} T^{F_3-F_2} \left(\frac{d\psi}{d\zeta}\right),$$

$$F_3 - F_2 = \frac{\alpha[(3 - \omega)(n + 1) - 2] - 6n}{2[\omega(n + 1) + 2]}, \tag{25}$$

where $\overline{(d\psi/d\zeta)}$ is the average value of the derivative of the thickness profile over the interval 0–1. The behaviour of the exponent $F_3 - F_2$ as a function of ω for given n , and of n for fixed ω , is qualitatively similar to that of F_3 , with the same critical values $\alpha_\omega = 2n/(n + 1)$ and $\alpha_n = \omega + 2$; for $\alpha = \alpha_\omega$, $F_3 - F_2 = -n/(n + 1)$; for $\alpha = \alpha_n$, $F_3 - F_2 = (1 - \omega)/2$. $F_3 - F_2$ is an increasing function of α for $\omega < \omega_1 = (3n + 1)/(n + 1)$, or, conversely, $n > n_1 = (\omega - 1)/(3 - \omega)$; the reverse is true for $\omega > \omega_1$ or $n < n_1$.

Fig. 2(a)–(f) display how F_2 , F_3 and $F_3 - F_2$ depend on ω for fixed $n = 0.5$ and on n for fixed $\omega = 1.5$; results for various values of α , including the critical ones, are shown. The two reference values ($n = 0.5$ and $\omega = 1.5$) are selected for illustrative purposes and represent common cases in natural porous media, i.e. a shear-thinning fluid and a permeability increasing with elevation from the bottom.

For a given fluid (fixed n), a current with a volume that remains constant ($\alpha = 0$) or increases moderately with time ($\alpha < \alpha_\omega$), becomes thinner ($F_3 < 0$) at a particular point as time increases. This type of current is thus confined to zones of high permeability for $\omega < 1$, and of low permeability for $\omega > 1$; as a consequence the propagation rate becomes lower as ω increases. Conversely, for $\alpha > \alpha_\omega$ the current height increases with time ($F_3 > 0$) and reaches zones of low permeability for $\omega < 1$, and of high permeability for $\omega > 1$; thus the propagation rate increases with ω . Consistently

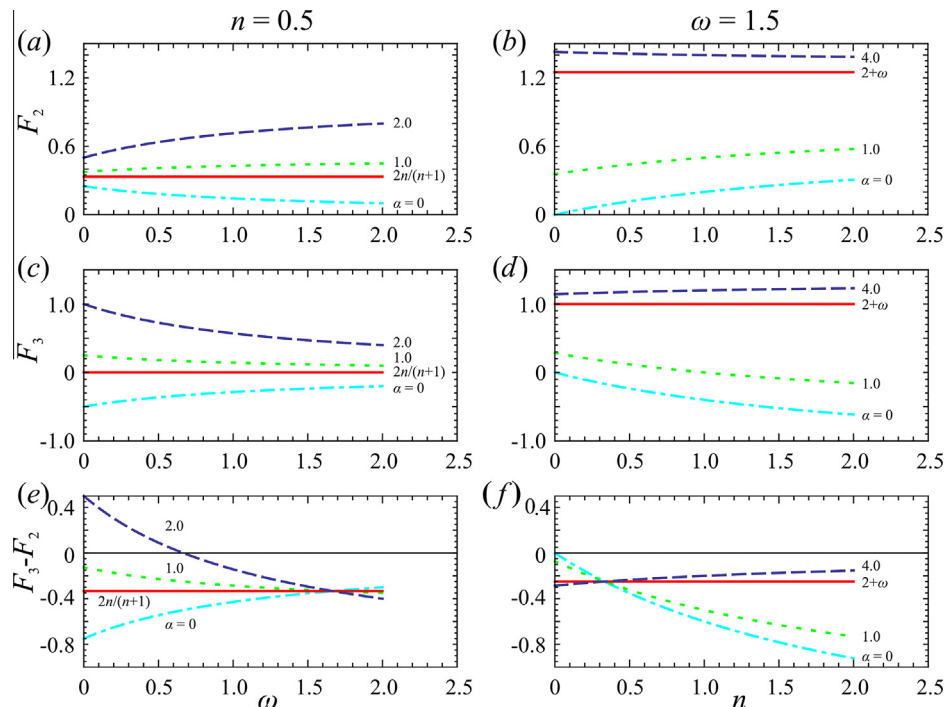


Fig. 2. (a)–(f) The value of the time exponents F_2 , F_3 and $F_3 - F_2$ for a current with length $\propto T^{F_2}$, height $\propto T^{F_3}$, mean free-surface gradient/aspect ratio $\propto T^{F_3-F_2}$, and volume $\propto T^\alpha$ in a porous medium with permeability varying vertically as $z^{\omega-1}$. Results are shown for F_2 , F_3 and $F_3 - F_2$ in the upper, intermediate and lower rows, respectively, as a function of ω for $n = 0.5$ and as a function of n for $\omega = 1.5$ (left and right columns, respectively), and for different values of α .

with the previous interpretation, for given α the average spatial gradient decreases with time ($F_3 - F_2 < 0$) when $\omega > \omega_2 = [\alpha(3n + 1) - 6n]/(\alpha(n + 1))$, and more so for larger ω . This implies a lower average resistance to the flow motion due to an increased average permeability. Qualitatively similar graphs are obtained with other reference values of n , except that the critical value α_{ω} increases with n .

When analyzing the behaviour of the time exponents for given permeability grading, different tendencies are observed. For positive grading ($\omega > 1$), it is seen that, for a less than critical volume increase with time ($\alpha < \alpha_n$), the gradient decreases with time ($F_3 - F_2 < 0$), more so for increasing n . This implies a reduced average resistance to the flow, which brings about an increase of the spreading rate (larger F_2) for larger values of n . For a rapidly increasing influx ($\alpha > \alpha_n$), the tendency is reversed and $F_3 - F_2$, though remaining negative, increases with n , implying in turn a modest decrease in the propagation rate F_2 as n increases. In homogeneous ($\omega = 1$) and negatively graded media ($\omega = 0.5$) the same trends with n are observed (not shown graphically), but

$F_3 - F_2$ takes on positive values for large enough α , indicating a gradient increasing with time due to increasing resistance to flow, as the current invades low-permeability zones.

For practical applications it is also of interest to determine if the current front is accelerating or decelerating. The speed of the current front is proportional to T^{F_2-1} , i.e., the current decelerates or accelerates depending on whether $\alpha < \alpha_l$ or $\alpha > \alpha_l$, where

$$\alpha_l = \frac{2[(\omega - 1)(n + 1) + 3]}{(\omega - 1)(n + 1) + 2}. \tag{26}$$

For a Newtonian fluid ($n = 1$), $\alpha_l = (2\omega + 1)/\omega$; for a homogeneous medium ($\omega = 1$), $\alpha_l = 3$.

To understand how the thickness profile affects the overall behaviour of the current via (25), in Fig. 3(a)–(f) we plot $\psi(\zeta)$ obtained by numerically integrating (17) with (19) and (24), for $\alpha = 0$ and 1 and various values of n and ω , selected to illustrate the cases of: (i) shear-thinning, Newtonian, and shear-thickening fluid; (ii) negative, null, and positive permeability grading with elevation. The analytical solution (20) for $\alpha = 0$ is perfectly repro-

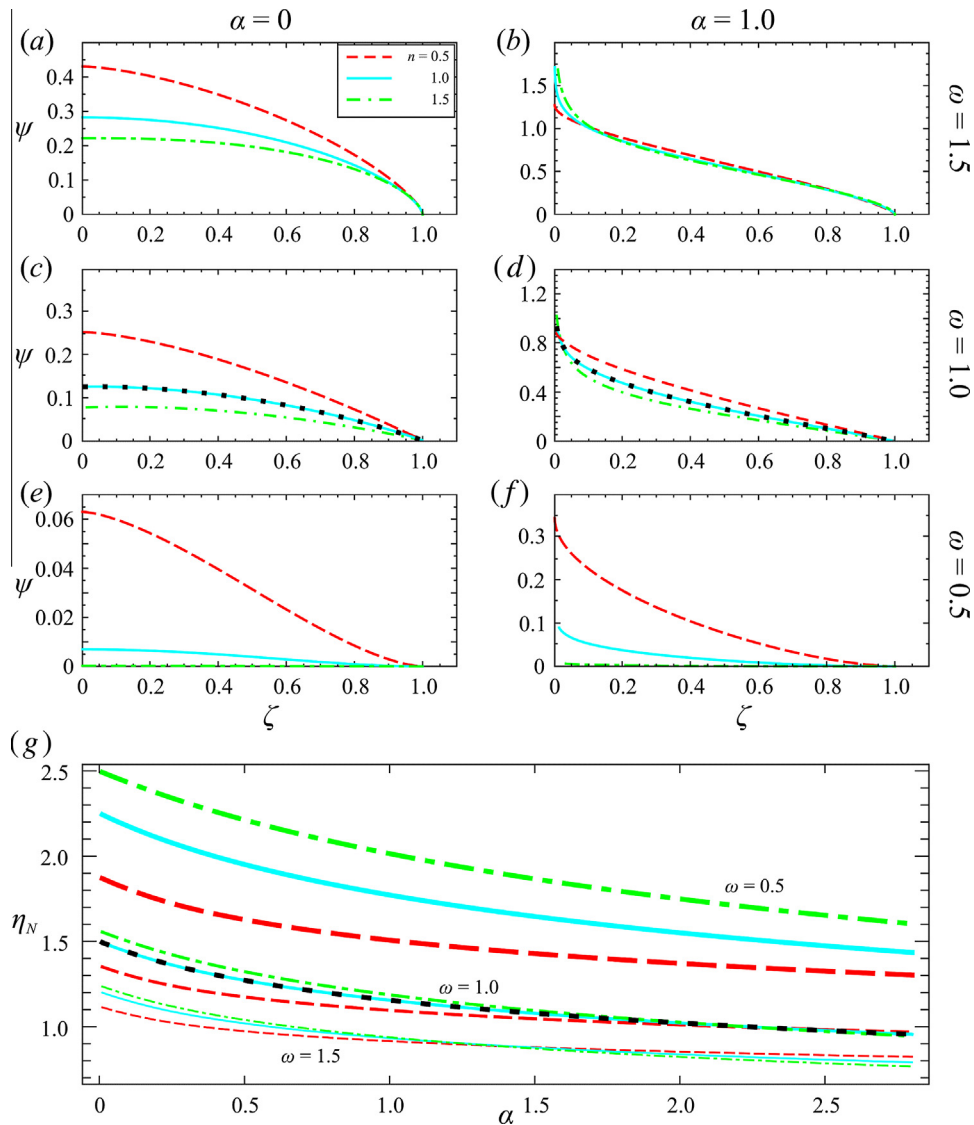


Fig. 3. (a)–(f) Thickness profile ψ as a function of the rescaled similarity variable ζ . Results are shown for vertically increasing, uniform, and vertically decreasing permeability (upper, intermediate, and lower rows, respectively), constant volume and constant flux release (left and right columns, respectively), and for shear-thinning (dashed red lines), Newtonian (solid light blue lines), and shear-thickening (dot-dashed green lines) fluids. (g) The similarity variable at the current front η_N versus α . Results derived by Lyle et al. [6] for $n = 1$ and $\omega = 1$ are also shown (dotted lines). (For interpretation of the references to colour in this figure legend, the reader is referred to the web version of this article.)

duced. Fig. 3(c) and (d) valid for a homogeneous medium were already presented by Longo et al. [32] and are included for comparison; they also demonstrate the coincidence of numerical results with the Newtonian results presented by Lyle et al. [6].

The thickness profile markedly increases with α for a given permeability variation and fluid, as the fluid volume released into the domain is larger; this effect is also observed for values of $\alpha > 1$ (not shown). For constant volume currents, the thickness profile is larger for shear-thinning ($n < 1$) than for Newtonian ($n = 1$) or shear-thickening fluids ($n > 1$). However the height of the currents also depends on η_N , whose behaviour, evaluated via (18), is presented in Fig. 3(g) as a function of α for various values of ω and n . The prefactor η_N is observed to increase with n and to decrease with α and ω , with a greater sensitivity for smaller values of ω and n . These tendencies are the opposite of those of the thickness profile. Inspection of Fig. 3 allows to analyze the average gradient of the thickness profile, which is seen to be lower for shear-thickening than for Newtonian or shear-thinning fluids. This effect is more evident for $\alpha = 0$, but it can be still observed for $\alpha = 1$ except near the origin, where the opposite is true (the spatial gradient of the thickness profile near the origin is of modest relevance since a limited quantity of fluid is contained there). The average gradient of the thickness profile also increases significantly for increasing ω .

The analysis of the dependency of the time exponents F_2 , F_3 and $F_3 - F_2$ of the current length, height, and average free-surface gradient, and of the thickness profile ψ and prefactor η_N , on problem parameters α , n , and ω , demonstrates that the current behaviour relies on the combined effects of depth, radius and resistance to flow. Depth and radius are constrained by mass balance while the flow resistance is modulated by the spatial gradient of the current and by the average permeability over the vertical. The actual radius and height of the current are best analyzed in dimensional coordinates upon employing (9). Overall, a reduction in the average spatial gradient of the current implies a decrease in the mean resistance to flow, whereas a reduction in the height of the current increases or decreases the resistance to flow depending whether $\omega > 1$ or $\omega < 1$. Hence if the height of the current decreases with time, as when the volume injected does not increase too rapidly: (i) in media with permeability increasing with elevation ($\omega > 1$), a limited reduction of the average spatial gradient is sufficient for the balance between the effect of the gradient and that of permeability; (ii) in media with permeability decreasing with elevation ($\omega < 1$), the reduction of the average gradient for

shear-thickening fluids must be strong enough to balance the increment of the flow resistance due to a flow field characterised by low permeability. If the latter condition is not satisfied, the average gradient increases and the hypotheses of the model are not respected.

In fact, limitations on the parameters and on the time of relevance emerge when considering the validity of the thin current approximation. The ratio between the average height \bar{H} of the current and its radius R_N is obtained from (16) and (14) as

$$\frac{\bar{H}}{R_N} = F_1^{3F_4} \eta_N^{F_5-1} T^{F_3-F_2} \bar{\psi}, \quad (27)$$

where $\bar{\psi}$ is the average value of the thickness profile over the interval 0–1. The validity of the approximation requires the former ratio to be lower than a small parameter ϵ_1 . Assigning a value to ϵ_1 allows deriving the upper limit value of α as a function of the time horizon T for given n and ω , or vice versa (see Section 2.2 in Ciriello et al. [2]). Asymptotically the thin current approximation requires $F_3 - F_2 < 0$, implying $\alpha[(3 - \omega)(n + 1) - 2] - 6n < 0$. As $\alpha \geq 0$, this relationship is satisfied for any α if $\omega > \omega_1 = (3n + 1)/(n + 1)$. If, on the other hand, $\omega < \omega_1$, a corresponding upper bound for α arises, given by

$$\alpha < \alpha_1 = \frac{6n}{(3 - \omega)(n + 1) - 2}. \quad (28)$$

For $n = 1$, $\omega_1 = 2$ and $\alpha_1 = 3/(2 - \omega)$; for $\omega = 1$, $\alpha_1 = 3$. Physically, for a rapid increase of the permeability along the vertical the current remains asymptotically thin for any type of injection; for a moderate vertical permeability gradient, an upper bound for the volume increase of the current with time is necessary for the aspect ratio of the current to remain small.

4. Experiments

The theoretical solution was tested against data from laboratory experiments conducted in the Hydraulics Laboratory of the University of Parma with currents of fluids with Newtonian and shear-thinning rheological behaviour with constant ($\alpha = 1.0$) and time-varying flux ($\alpha = 1.5$ and 2.0). Air was the ambient fluid in all cases. The experimental protocol and setup (shown in Fig. 4) described here were earlier adopted by Longo et al. [32] to conduct tests with shear-thinning fluids in a homogeneous porous

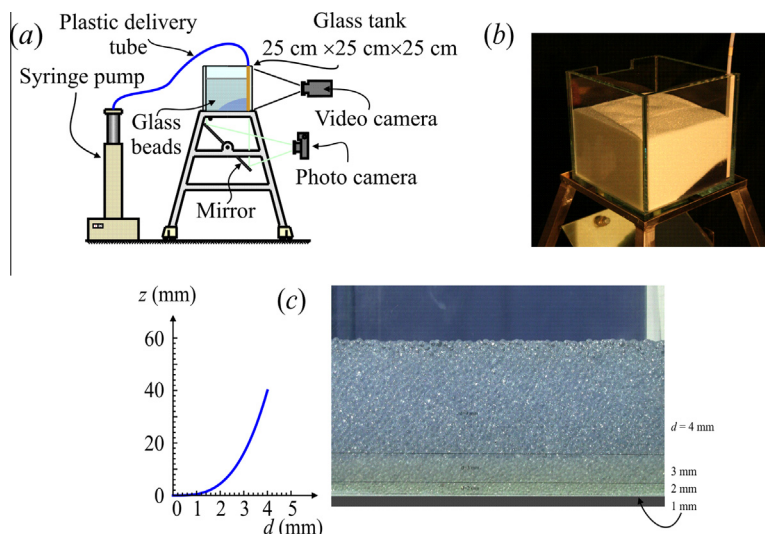


Fig. 4. (a) Experimental setup. (b) Picture of the glass tank at the end of a test. (c) Stratification of glass beads used to reproduce increasing permeability along the vertical axis.

medium; their result complement the present set of experiments and validate the model for $\omega = 1$. Further experimental support for homogeneous media and Newtonian fluids ($n = 1$) is provided by the work of Lyle et al. [6]. Here, no tests were conducted with $\omega < 1$ or $n > 1$, as these cases are less common.

4.1. Experimental protocol and setup

The experiments were performed in a 90°-sector glass tank filled with glass beads to create a porous medium with permeability varying along the vertical. The continuous vertical gradient of the permeability implicit in (1) was approximately reproduced in the laboratory by superimposing a sequence of strata of beads, each stratum having beads of uniform diameter. The link between the theoretical parameters k_0 and ω and the geometry and properties of the experimental setting is illustrated in Appendix B. The intruding fluid was injected through a quarter-cylinder volume of radius ≈ 10 mm positioned vertically at one corner of the tank, having permeable walls constructed with a brass net. The outflow section of the plastic tube delivering the fluid was located near the solid floor of the tank. While this arrangement resembles a point source, the well-like structure obtained with the brass net favored an injection distributed along the vertical. Two different syringe pumps, with accuracies of 0.5% and 1% of the instantaneous discharge, were used. The first pump was controlled with an analogue electric signal to generate a time-increasing influx ($\alpha = 1.5, 2.0$). The lateral current profile was recorded continuously using a high-resolution video camera, and the radial spreading was recorded by a photo camera shooting from below through a mirror. The images were processed to obtain a planar restitution and detect the boundary of the intruding current, with an overall accuracy of ± 1 mm. Six experiments were conducted with a mixture of water and glycerol that was Newtonian in nature. Six additional experiments were carried out using a suspension of Xanthan gum in a mixture of water and glycerol that exhibited shear-thinning behaviour. A set of eleven experiments were earlier performed with shear-thinning and Newtonian fluids in a homogeneous medium ($\omega = 1$), as reported in Longo et al. [32]. Ink was added to the intruding fluid to increase the contrast and facilitate the detection of the interface. The rheological parameters of the intruding fluids were evaluated with two strain-controlled rheometers at a temperature approximately equal to that measured at the end of each experiment ($\Theta = 25$ °C for the first six tests and $\Theta = 28$ °C for the last six tests). The descriptive parameters for each experiment are summarised in Table 1. Two videos recorded for experiments 14 and 19 are also available in the Supplementary Material.

Table 1

Parameter values used for all experiments. The superscript *a* indicates availability of a recorded video as Supplementary Material. The superscript *b* indicates that a 1%-accuracy pump that was built in the laboratory was used. All other experiments were conducted with a pump of 0.5% accuracy. $Q' = \alpha Q t^{\alpha-1}$ denotes the full-circle volumetric discharge. The porosity was assumed to be $\phi = 0.37$. This is an average value for closed packed ballotini, as measured in [6], also consistent with specific measurements by Aste et al. [33], Bloom et al. [34] and Ribeiro et al. [35]. The rheological parameters were obtained by direct rheometric measurements at $\Theta = 25$ °C in the range of 0.1–5 s⁻¹ except for experiments 22–27, for which the temperature was $\Theta = 28$ °C.

Exp.	α	d (mm)	m (Pa s ^{<i>n</i>})	n	$\Delta\rho$ (kg m ⁻³)	Q' (ml s ⁻¹)	ω	k_0 (10 ⁻⁹ m ²)
13	1.0	1.0–4.0	0.60	0.33	1175	0.40	1.63	4.99
14 ^a	1.5	1.0–4.0	0.60	0.33	1175	$0.078 \cdot t^{1/2}$	1.63	3.47
15	2.0	1.0–4.0	0.60	0.33	1175	$0.032 \cdot t$	1.63	4.57
19 ^a	1.0	1.0–4.0	0.28	1.00	1241	0.40	1.63	9.63
20	1.5	1.0–4.0	0.28	1.00	1241	$0.06 \cdot t^{1/2}$	1.63	8.14
21	2.0	1.0–4.0	0.28	1.00	1241	$0.032 \cdot t$	1.63	9.87
22 ^b	1.0	1.0–4.0	0.67	0.42	1175	0.550	1.63	8.97
23 ^b	1.0	1.0–4.0	0.67	0.42	1175	0.677	1.63	9.37
24 ^b	1.0	1.0–4.0	0.67	0.42	1175	0.866	1.63	9.85
25 ^b	1.0	1.0–4.0	0.14	1.00	1241	0.535	1.63	8.43
26 ^b	1.0	1.0–4.0	0.14	1.00	1241	0.704	1.63	9.00
27 ^b	1.0	1.0–4.0	0.14	1.00	1241	0.888	1.63	9.51

In examining the experimental profile, a correction was applied to the raw data to consider the capillary rise and the meniscus at the glass wall according to the methodology described in Longo et al. [32]. A Particle Image Velocimetry analysis performed with a macro-lens detected no motion of the glass beads in the entire flow domain, ruling out dilatancy effects.

4.2. Experimental results

The scaled non-dimensional results for the current front position (relative to an origin located at the corner of the tank) are plotted with respect to time in log–log scale in Fig. 5(a) for all experiments. The model fit on a linear scale is shown for experiment 27 in Fig. 6. The experimental results collapse onto the theoretical lines, except at early time, indicating a satisfactory prediction of the power of time F_2 and pre-multiplicative factor η_N given by (14) and (21) for both constant ($\alpha = 1$) and increasing ($\alpha = 1.5, 2$) influx. Fig. 5(b) depicts the dimensionless thickness profile at various times for a selected test with variable influx (experiment 19). Fig. 5(c) presents the experimental versus theoretical thickness profile for all experiments and a single time value, corresponding to the last available shot for each experiment. Both figures demonstrate that the experimental results tend to collapse onto the theoretical predictions of the similarity solution, with larger deviations near the origin and front end. These are confirmed upon examining results for individual tests (see Fig. 7 for experiment 13, and the Supplementary Material for all other experiments). The relatively poor fit near the origin can be ascribed to (i) boundary effects due to the finite-sized injection cylinder, (ii) injection tube located near the bottom of the tank rather than along the entire vertical edge, and (iii) neglecting the vertical velocity, which is locally comparable to the horizontal velocity. The effect of the finite size well are negligible given its small radius. Local effects due to the position of the injection point are relevant in the near field $\zeta < 0.2$, as already observed in some of the experiments shown in Fig. A.1 by Lyle et al. [6]; however the arrangement adopted in the present experiments, featuring a well-like structure, likely mitigates the discrepancies with the similarity solution. We therefore surmise that the presence of vertical Darcy velocities, that are neglected in the model, significantly contributes to deviations from theoretical results near the injection point. Near the front end of the current, deviations from the theory are mainly due to the discretisation adopted in the experiments, where the continuous permeability profile given by (1) is approximated superimposing different layers of particles, each layer having uniform diameter. The experimental result correspond more closely to theory for the radius of propagation than for the profile

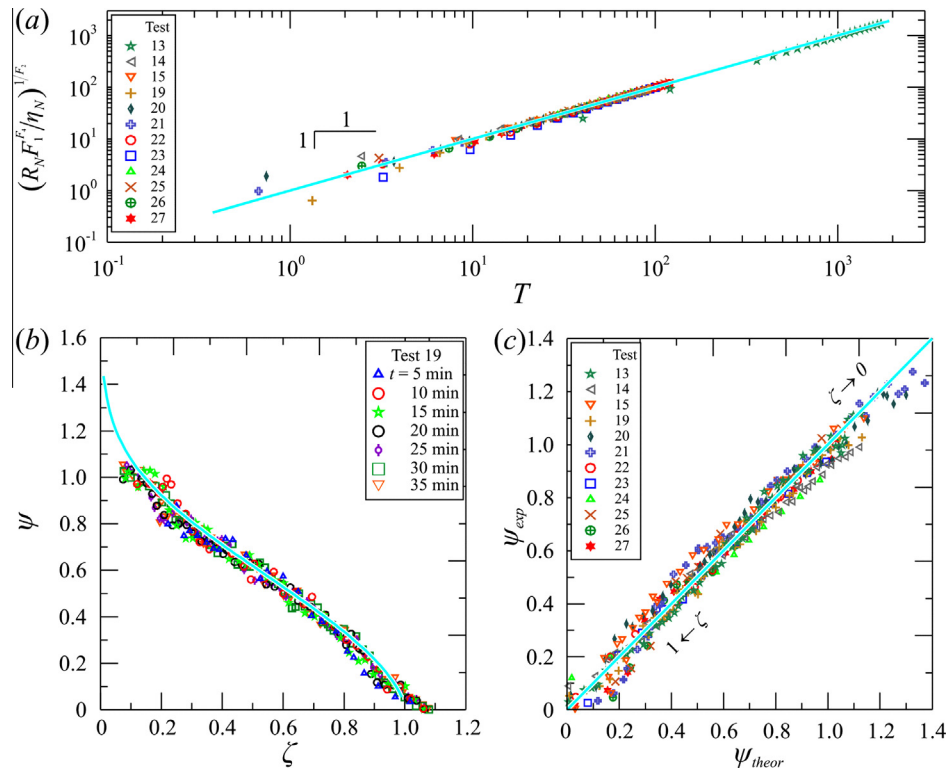


Fig. 5. Experimental results (symbols) versus theoretical results (solid curves). (a) The scaled non-dimensional front position versus dimensionless time (one point of every two is plotted). (b) Thickness profile at various times versus the reduced similarity variable for experiment 19 with time-increasing influx of a shear-thinning fluid. (c) The experimental versus theoretical thickness profile for all experiments, indicating the profile measured at a time corresponding to the last available shot.

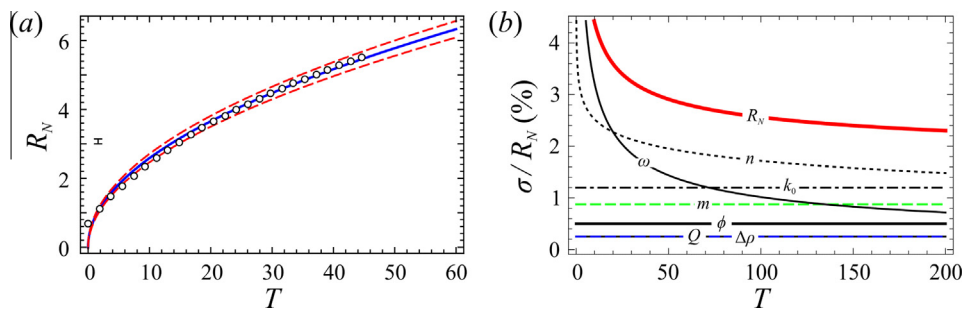


Fig. 6. (a) The radius of the front end of the current as a function of time for test 27. The thick line is the theoretical prediction, the symbols are the experimental results, and the dashed lines are the 95% confidence limits. The error bar representing the experimental error at 95% confidence level in detecting the front position is indicated for comparison on the l.h.s. (b) The coefficient of variation of the radius and the contributions of the individual parameters as a function of time. Test 27, $m = 0.14 \pm 3.5\%$ Pa s⁻¹, $n = 1.0 \pm 3.5\%$, $\Delta\rho = 1241 \pm 1.0\%$ kg m⁻³, $Q' = 0.888 \pm 1.0\%$ ml s⁻¹, $\alpha = 1.0$, $\phi = 0.37 \pm 1\%$, $\omega = 1.63 \pm 4.3\%$, $k_0 = 9.51 \cdot 10^{-9} \pm 4.8\%$ m².

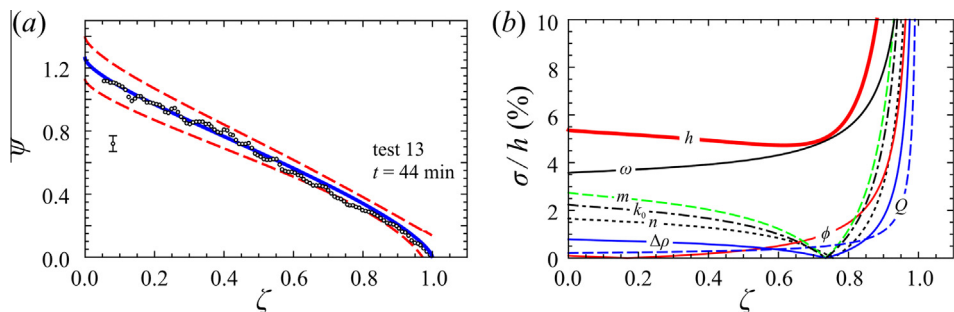


Fig. 7. (a) Thickness profile of the current at time $t = 44$ min for test 13. The thick line is the theoretical prediction, the dots are the experimental results, and the dashed lines are the 95% confidence limits. The error bar on the l.h.s. is the experimental error in detecting the profile at the 95% confidence level. (b) The coefficient of variation of the profile and the contributions of the individual parameters. Test 13, $m = 0.60 \pm 3.5\%$ Pa s⁻¹, $n = 0.33 \pm 3.5\%$, $\Delta\rho = 1175 \pm 1\%$ kg m⁻³, $Q' = 0.40 \pm 0.5\%$ ml s⁻¹, $\phi = 0.37 \pm 1\%$, $\omega = 1.63 \pm 4.3\%$, and $k_0 = 4.99 \cdot 10^{-9} \pm 4.8\%$ m².

because the current front was evaluated as the spatial average of the current boundary in the images taken from below.

4.3. Uncertainty analysis

An uncertainty analysis was undertaken to quantify the agreement between the theoretical and experimental values of the radius r_N and height h of the current. The generic model output i , with $i = r_N, h$, is a function of the two independent variables r and t and of model parameters $j = m, n, \Delta\rho, Q, \phi, \omega, k_0$. Thus, the total uncertainty in i was obtained by combining in quadrature the contribution of the uncertainties in the parameters as

$$\sigma_i^2 = \left(\frac{\partial h}{\partial m}\right)^2 \sigma_m^2 + \left(\frac{\partial h}{\partial n}\right)^2 \sigma_n^2 + \dots, \quad (29)$$

where the σ^2 symbol denotes the variance, which is assumed to be an estimate of the uncertainty. A standard deviation σ_j was attributed to each model parameter using available information: a separate statistical analysis was performed on the rheometric data to infer σ_m and σ_n , while the manufacturer's specifications were employed for the diameter of the glass beads and the flow rate of the pumps used in the experiments. A coefficient of variation equal to 1% was assumed for the porosity and the density, whereas the uncertainties in ω and k_0 were computed by assuming a coefficient of variation of 10% and 5% respectively for the minimum and maximum bead diameter among those used, and equal to 10% for the total thickness of the bead layers. This approach resulted in a coefficient of variation of 4.3% for ω and 4.8% for k_0 . We further assumed that the acceleration due to gravity and the parameter α were known with certainty.

Fig. 6(a) depicts, in dimensionless form, the theoretical and experimental radius of the current as a function of time for test 27; the error bands at the 95% confidence limit, and the error bars are also shown. The agreement between model predictions and experimental results is almost perfect, except at early times, when the experimental setup and injection process induced some discrepancies. Fig. 6(b) illustrates the contributions to the coefficient of variation of the radius deriving from the uncertainty in the parameters. It is seen that the highest coefficient of variation is associated to n and ω , followed asymptotically by the reference permeability k_0 .

Fig. 7(a) presents a comparison of the theoretical and experimental thickness profile at given time for test 13; the 95% confidence limits and the error bars are shown. Because the difference between the estimation of the experimental points and the theoretical profile contains zero, the experimental data and theoretical profile can be considered statistically equal with a 95% level of confidence. Fig. 7(b) presents the contributions of the uncertainties associated with model parameters. The most relevant contribution is due to the exponent ω , which accounts for more than 50% of the coefficient of variation of the thickness profile. This significant result confirms that the spatial heterogeneity of the porous medium is a crucial factor controlling the spreading of the current.

A similar uncertainty analysis was conducted for all tests listed in Table 1; the Supplementary Material reports the comparison between the experimental and theoretical thickness profile for all tests. The agreement between the theoretical and experimental results is largely satisfactory, except (for some experiments) near the origin and front end, as noted earlier. The theoretical and experimental results match more closely for slow currents than for fast currents.

5. Conclusions

We theoretically and experimentally investigated the behaviour of axisymmetric gravity currents of power-law fluids of rheological index n in a porous medium with a continuous vertical permeabil-

ity variation described by the parameter ω . The rate of propagation of a current of volume $V \sim t^\alpha$ and the appropriate scaling for its shape were determined as functions of α , ω , and n by using similarity variables. Two critical values for the volume parameter, $\alpha_\omega = 2n/(n+1)$ and $\alpha_n = \omega + 2$, govern the tendency of the time exponents F_2 and F_3 of the radius and height of the gravity current to increase or decrease with n and ω ; a third critical value α_l dictates if the current accelerates or decelerates; a fourth critical value α_1 governs the asymptotic validity of the thin current approximation. The second, third and fourth values are distinct, unlike the case of Newtonian gravity currents in uniform media. The physical explanation of the current behaviour relies on the combined effects of depth, radius and resistance to flow. Depth and radius are constrained by mass balance, while the flow resistance is modulated by the spatial gradient of the current and by the average permeability on the vertical. For example, the response of the current to a shear-thickening fluid ($n > 1$) is a reduction of the average spatial gradient with a counteracting effect represented by a reduced thickness for $\omega > 1$ (or increased thickness for $\omega < 1$) or a concurrent effect in the opposite case. The actual behaviour of the current in terms of radius and height is best analyzed in dimensional coordinates.

In the laboratory, the vertical gradient of the permeability was reproduced by superimposing a sequence of uniform strata of glass beads. The experimental results for constant- and variable-flux gravity currents agree well with the theoretical predictions for both the front position and current profile. Deviations from theory occur near the origin and at the front end of the current. The former are due to the assumption of negligible vertical velocity and to boundary effects; the latter can be attributed to the discretisation, adopted in the experiments, of the continuous permeability profile.

An analysis based on the actual uncertainties affecting problem parameters indicated that the fluid behaviour index n and the permeability variation factor ω have the greatest impact on results.

Results obtained show that the rheological nature of the intruding fluid and permeability variations significantly affect the radius and profile of gravity-driven currents propagating in porous media. In turn, the prediction of the extension and shape of the current for an instantaneous or continuous injection is relevant in contamination problems and remediation efforts involving non-Newtonian fluids. More complex and realistic patterns of spatial permeability variations, as well as the behaviour of rheologically complex fluids not adequately described by the power-law model, can be explored based on these results.

Acknowledgements

Support from Università di Bologna RFO (Ricerca Fondamentale Orientata) 2011 and 2012 is gratefully acknowledged. We are grateful to the editor and the reviewers for their comments, which improved substantially the quality of the manuscript.

Appendix A. The special case $\alpha = 3$

In the special case $\alpha = 3$, the non-dimensional expression (10) breaks down due to the absence of the characteristic time scale defined in (9). In addition, a second natural velocity scale $(Q/\phi)^{1/3}$ arises. An arbitrary time scale \tilde{t}^* and a new spatial length scale $\tilde{r}^* = (Q/\phi)^{1/3}\tilde{t}^*$ are thus defined, and dimensionless variables become $\tilde{T} = t/\tilde{t}^*$; $\tilde{R} = r/\tilde{r}^*$; $\tilde{R}_N = r_N/\tilde{r}^*$; $\tilde{H} = h/\tilde{r}^*$. In these new variables, the problem is stated as

$$\frac{\delta_r}{F_1} \frac{1}{\tilde{R}} \frac{\partial}{\partial \tilde{R}} \left(\tilde{R} \tilde{H}^{F_1} \left| \frac{\partial \tilde{H}}{\partial \tilde{R}} \right|^{1/n-1} \frac{\partial \tilde{H}}{\partial \tilde{T}} \right) = \frac{\partial \tilde{H}}{\partial \tilde{T}}, \quad (A.1)$$

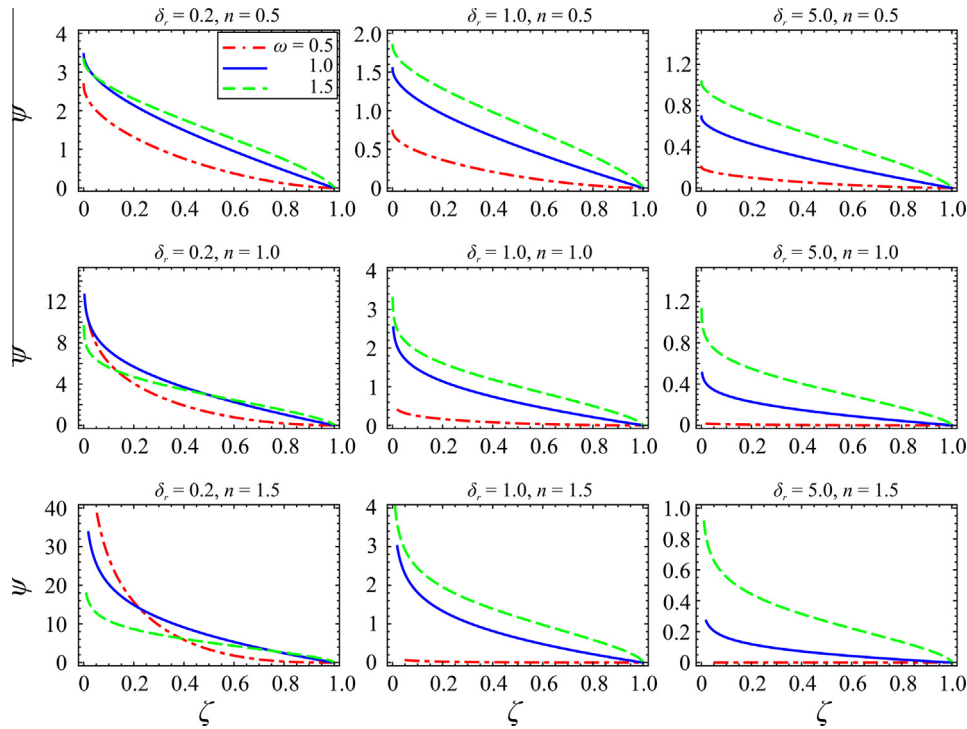


Fig. A.1. Thickness profile for $\alpha = 3$, $\delta_r = 0.2, 1.0, 5.0$, $n = 0.5, 1.0, 1.5$, and $\omega = 0.5, 1.0, 1.5$.

$$2\pi \int_0^{\tilde{R}_N} \tilde{H} \tilde{R} d\tilde{R} = \tilde{T}^3, \quad (\text{A.2})$$

where $\delta_r = v^*/(Q/\phi)^{1/3}$ is the ratio between the velocity scale in (9) and the new velocity scale. Physically, δ_r represents the ratio between the factors favouring the current spreading (density difference $\Delta\rho$, domain reference permeability k_0 , and reciprocal of fluid consistency index m) and the source strength. Defining the self-similar variable as $\eta = F_1^{F_4} \tilde{R} \tilde{T}^{-F_2}$, with

$$F_1 = \frac{(\omega - 1)(n + 1) + 2n}{2n}, \quad F_2 = \frac{3\omega(n + 1) + 3 - n}{2[\omega(n + 1) + 2]}, \quad (\text{A.3})$$

$$F_4 = \frac{n}{\omega(n + 1) + 2}$$

and performing the same mathematical transformations as in the general case, the height of the current becomes

$$\tilde{H}(\tilde{R}, \tilde{T}) = F_1^{2F_4} \eta_N^{F_3} \tilde{T}^{F_3} \psi(\zeta), \quad \zeta = \eta/\eta_N, \quad (\text{A.4})$$

in which

$$F_3 = \frac{n + 3}{\omega(n + 1) + 2}, \quad F_5 = \frac{2(n + 1)}{(\omega - 1)(n + 1) + 2} \quad (\text{A.5})$$

and the thickness profile ψ is the solution of the following nonlinear o.d.e.:

$$\delta_r (\zeta \psi^{F_1} |\psi'|^{1/n-1} \psi')' + F_2 \zeta^2 \psi' - F_3 \zeta \psi = 0 \quad (\text{A.6})$$

with $\psi(1) = 0$. The second boundary condition needed for the numerical integration of (A.6) is obtained in analogy with the general case as:

$$\psi'(\zeta \rightarrow 1) = -a_0 b e^{b-1}, \quad a_0 = \left[\frac{F_2}{\delta_r b^{1/n-1} (bF_1 + \frac{b-1}{n})} \right]^{nb},$$

$$b = \frac{1}{1 - n(1 - F_1)}, \quad (\text{A.7})$$

where ϵ is a small quantity. Fig. A.1 depicts the thickness profile for various values of the parameters δ_r , n , ω . Graphical results for a homogeneous medium ($\omega = 1$), $n = 0.50, 1.50$, and $\delta_r = 0.2, 1, 5$ replace those shown in Fig. 9 of [8]. It is seen that an increase in δ_r produces a decrease in the thickness profile and vice versa; the impact of the actual value of δ_r is larger for shear-thickening than for shear-thinning fluids.

For $\omega = 1$, the factors simplify to $F_1 = 1$, $F_2 = 1$, $F_3 = 1$, $F_4 = n/(n + 3)$, and $F_5 = n + 1$ and the governing equations and the boundary conditions reduce to the simpler counterparts derived in Eqs. (31) and (A.8) of Di Federico et al. [8] for axisymmetric non-Newtonian gravity currents in homogeneous porous media. Note that the sign of the last term in Eq. (31) of [8] is erroneous and should be changed to positive, thus becoming consistent with the more general case represented by (A.6). For $n = 1$, novel results for Newtonian radial gravity currents flowing in vertically graded media with volume increasing as time cubed are derived. In this case $F_1 = \omega$, $F_2 = (3\omega + 1)/[2(\omega + 1)]$, $F_3 = 2/(\omega + 1)$, $F_4 = 1/[2(\omega + 1)]$, and $F_5 = 2/\omega$. When comparing the value of α_1 defined in (28) with the present special case, it is seen that the currents with $\alpha = 3$ are accelerated for $\omega > 1$, have a constant front speed for $\omega = 1$, and are decelerated for $\omega < 1$. The thin current approximation is asymptotically valid only for $\omega \leq 1$.

Appendix B. The parameters of vertical permeability variation

This Appendix illustrates the relationship between the theoretical parameters of the power-law permeability variation (1) and the discrete sequence of strata of beads with uniform diameter used in the experiments. First, a preliminary evaluation of the maximum height of the intruding current is performed for each test, and the overall thickness of the porous medium Δ is conveniently adjusted to ensure that the advancing current is contained within the porous medium. Then the diameter of the beads is determined according to the following method. Taking the logarithm of (1) yields

$$\log(k) = \log(k_0) + (\omega - 1) \log(z/r^*). \quad (\text{B.1})$$

The length scale r^* is equal to (see (9))

$$r^* = \left(\frac{Q}{\phi}\right)^{1/(3-\alpha)} \left[\frac{(\Delta \rho g)^{1/n}}{\phi}\right]^{-\alpha/(3-\alpha)} k_0^{-\alpha(n+1)/[2n(3-\alpha)]}, \quad (\text{B.2})$$

hence results

$$\log(k) = \left[1 + \frac{(\omega - 1)\alpha(n + 1)}{2n(3 - \alpha)}\right] \log(k_0) + (\omega - 1) \log(z/c), \quad (\text{B.3})$$

where

$$c = \left(\frac{Q}{\phi}\right)^{1/(3-\alpha)} \left[\frac{(\Delta \rho g)^{1/n}}{\phi}\right]^{-\alpha/(3-\alpha)}. \quad (\text{B.4})$$

According to the Kozeny–Carman equation, the permeability of a uniform stratum of beads with diameter d and porosity ϕ is given by $k = \phi^3 d^2 / [180(1 - \phi)^2]$. Requiring that the permeability correspondent to the minimum diameter of the beads $d = d_{min}$ is reached at $z = d_{min}/2$, and the permeability correspondent to the maximum diameter of the beads $d = d_{max}$ is reached at $z = \Delta$, the two unknowns ω and k_0 can be derived solving the following system of equations

$$\begin{cases} \log(k_{min}) = \left[1 + \frac{(\omega - 1)\alpha(n + 1)}{2n(3 - \alpha)}\right] \log(k_0) + (\omega - 1) \log((d_{min}/2)/c), \\ \log(k_{max}) = \left[1 + \frac{(\omega - 1)\alpha(n + 1)}{2n(3 - \alpha)}\right] \log(k_0) + (\omega - 1) \log(\Delta/c), \end{cases} \quad (\text{B.5})$$

where $k_{min} = \phi^3 d_{min}^2 / [180(1 - \phi)^2]$ and $k_{max} = \phi^3 d_{max}^2 / [180(1 - \phi)^2]$. Subtracting the two equations results in

$$\omega = 1 + \frac{\log(k_{min}/k_{max})}{\log((d_{min}/2)/\Delta)}, \quad (\text{B.6})$$

in which ω depends only on the diameters of the beads, the porosity ϕ , and Δ . The solution for k_0 reveals that this parameter varies with all other parameters controlling the spread of the intruding current.

In the present experiments we selected $d_{min} = 1$ mm, $d_{max} = 4$ mm, $\Delta = 40$ mm, $\phi = 0.37$, obtaining $\omega = 1.63$ and the

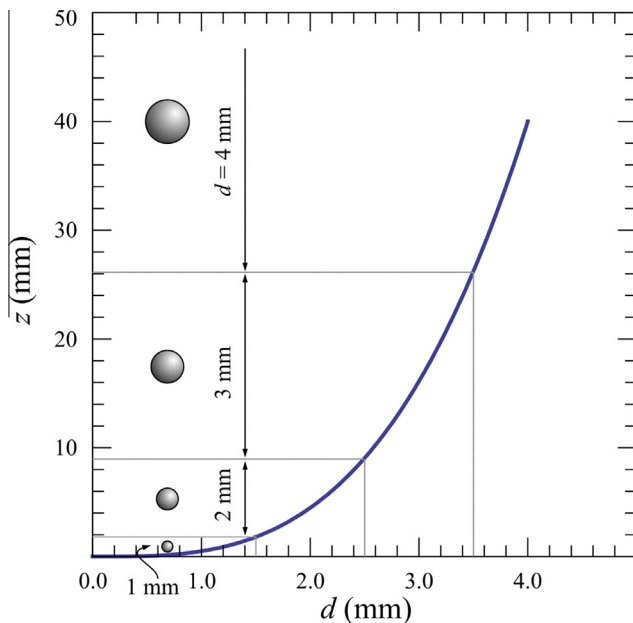


Fig. B.1. Vertical variation of the beads diameter.

corresponding variation of permeability with elevation. Equating (1) with the Kozeny–Carman equation, the function $d = d(z)$ was derived. The thickness of the intermediate layers was obtained from the inverse of the latter function, computed at the available commercial values of the beads diameter, as shown in Fig. B.1.

Appendix C. Supplementary data

Supplementary data associated with this article can be found, in the online version, at <http://dx.doi.org/10.1016/j.advwatres.2014.04.015>.

References

- [1] Lake L. *Enhanced oil recovery*. Prentice Hall; 1989.
- [2] Ciriello V, Di Federico V, Archetti R, Longo S. Effect of variable permeability on the propagation of thin gravity currents in porous media. *Int. J. Non-Linear Mech.* 2013;57:168–75. <http://dx.doi.org/10.1016/j.ijnonlinmec.2013.07.003>.
- [3] Werner A, Bakker M, Post V, Vandenboehede A, Lu C, Ataie-Ashtiani B, Simmons C, Barry D. Seawater intrusion processes, investigation and management: recent advances and future challenges. *Adv Water Resour* 2013;51:3–26. <http://dx.doi.org/10.1016/j.advwatres.2012.03.004>.
- [4] Huppert HE, Neufeld JA, Strandkvist C. The competition between gravity and flow focusing in two-layered porous media. *J Fluid Mech* 2013;720:5–14. <http://dx.doi.org/10.1017/jfm.2012.623>.
- [5] Huppert HE, Woods AW. Gravity-driven flows in porous layers. *J Fluid Mech* 1995;292:55–69. <http://dx.doi.org/10.1017/S0022112095001431>.
- [6] Lyle S, Huppert H, Hallworth M, Bickle M, Chadwick A. Axisymmetric gravity currents in a porous medium. *J Fluid Mech* 2005;543:293–302. <http://dx.doi.org/10.1017/S0022112005006713>.
- [7] Di Federico V, Archetti R, Longo S. Similarity solutions for spreading of a two-dimensional non-Newtonian gravity current. *J Non-Newtonian Fluid Mech* 2012;177–178:46–53. <http://dx.doi.org/10.1016/j.jnnfm.2012.04.003>.
- [8] Di Federico V, Archetti R, Longo S. Spreading of axisymmetric non-Newtonian power-law gravity currents in porous media. *J Non-Newtonian Fluid Mech* 2012;189–190:31–9. <http://dx.doi.org/10.1016/j.jnnfm.2012.10.002>.
- [9] Savins JG. Non-Newtonian flow through porous media. *Ind Eng Chem* 1969;61:18–47. <http://dx.doi.org/10.1021/ie50718a005>.
- [10] Hamed S, Belhadri M. Rheological properties of biopolymers drilling fluids. *J Petrol Sci Eng* 2009;67:84–90. <http://dx.doi.org/10.1016/j.petrol.2009.04.001>.
- [11] Livescu S. Mathematical modeling of thixotropic drilling mud and crude oil flow in wells and pipelines – a review. *J Petrol Sci Eng* 2012;98–99:174–84. <http://dx.doi.org/10.1016/j.petrol.2012.04.026>.
- [12] Tosco T, Sethi R. Transport of non-Newtonian suspensions of highly concentrated micro-and nanoscale iron particles in porous media: a modeling approach. *Environ Sci Technol* 2010;44:9062–8. <http://dx.doi.org/10.1021/es100868n>.
- [13] Ciriello V, Di Federico V. Similarity solutions for flow of non-Newtonian fluids in porous media revisited under parameter uncertainty. *Adv Water Resour* 2012;43:38–51. <http://dx.doi.org/10.1016/j.advwatres.2012.03.028>.
- [14] Alehossein H. Viscous, cohesive, non-Newtonian, depositing, radial slurry flow. *Int J Miner Process* 2009;93:11–9. <http://dx.doi.org/10.1016/j.minpro.2009.04.006>.
- [15] Hong J, F. (Ceji), Lin H, Tan W. Non-Newtonian effects on low-density lipoprotein transport in the arterial wall. *J Non-Newtonian Fluid Mech* 2012;189–190:1–7. <http://dx.doi.org/10.1016/j.jnnfm.2012.09.008>.
- [16] Ortega J. A porous media model for blood flow within reticulated foam. *Chem Eng J* 2013;99:59–66. <http://dx.doi.org/10.1016/j.ces.2013.05.025>.
- [17] Sochi T. Flow of non-Newtonian fluids in porous media. *J Polym Sci Part B Polym Phys* 2010;48(23):2437–767. <http://dx.doi.org/10.1002/polb.22144>.
- [18] Longo S, Di Federico V, Archetti R, Chiapponi L, Ciriello V, Ungarish M. On the axisymmetric spreading of non-newtonian power-law gravity currents of time-dependent volume: an experimental and theoretical investigation focused on the inference of rheological parameters. *J Non-Newtonian Fluid Mech* 2013;201:69–79. <http://dx.doi.org/10.1016/j.jnnfm.2013.07.008>.
- [19] Anderson DM, McLaughlin RM, Miller CT. The averaging of gravity currents in porous media. *Phys Fluids* 2003;15(10):2810–29. <http://dx.doi.org/10.1063/1.1600733>.
- [20] Zheng Z, Soh B, Huppert HE, Stone HA. Fluid drainage from the edge of a porous reservoir. *J Fluid Mech* 2013;718:558–68. <http://dx.doi.org/10.1017/jfm.2012.630>.
- [21] Fadili A, Tardy P, Pearson J. A 3D filtration law for power-law fluids in heterogeneous porous media. *J Non-Newtonian Fluid Mech* 2002;106:121–46. [http://dx.doi.org/10.1016/S0377-0257\(02\)00085-X](http://dx.doi.org/10.1016/S0377-0257(02)00085-X).
- [22] Marsily GD. *Hydrogéologie quantitative*. Masson; 1980.
- [23] Jiang X-W, Wang X-S, Wan L. Semi-empirical equations for the systematic decrease in permeability with depth in porous and fractured media. *Hydrogeol J* 2010;18(4):839–50. <http://dx.doi.org/10.1007/s10040-010-0575-3>.
- [24] Sen Z. Radial flow in vertically graded hydraulic conductivity aquifers. *J Hydraul Eng* 1989;115(12):1667–82. [http://dx.doi.org/10.1061/\(ASCE\)0733-9429\(1989\)115:12\(1667\)](http://dx.doi.org/10.1061/(ASCE)0733-9429(1989)115:12(1667)).

- [25] Mathunjwa J, Hogg A. Freely draining gravity currents in porous media: dipole self-similar solutions with and without capillary retention. *Eur J Appl Math* 2007;18:337–62. <http://dx.doi.org/10.1017/S0956792507006985>.
- [26] Bird RB, Stewart WE, Lightfoot EN. *Transport phenomena*. John Wiley & Sons; 1960.
- [27] Christopher RH, Middleman S. Power-law flow through a packed tube. *Ind Eng Chem Fundam* 1965;4:422–7. <http://dx.doi.org/10.1021/i160016a011>.
- [28] Shenoy AV. Non-Newtonian fluid heat transfer in porous media. *Adv Heat Trans* 1995;24:102–90. [http://dx.doi.org/10.1016/S0065-2717\(08\)70233-8](http://dx.doi.org/10.1016/S0065-2717(08)70233-8).
- [29] Pascal H. Nonsteady flow of non-Newtonian fluids through a porous medium. *Int J Eng Sci* 1983;21:199–210.
- [30] Vella D, Huppert HE. Gravity currents in a porous medium at an inclined plane. *J Fluid Mech* 2006;555:353–62. <http://dx.doi.org/10.1017/S0022112006009578>.
- [31] Pattle RE. Diffusion from an instantaneous point source with a concentration-dependent coefficient. *Q J Mech Appl Math* 1959;4:407–9. <http://dx.doi.org/10.1093/qjmam/12.4.407>.
- [32] Longo S, Di Federico V, Chiapponi L, Archetti R. Experimental verification of power-law non-Newtonian axisymmetric porous gravity currents. *J Fluid Mech* 2013;731(R2):1–12. <http://dx.doi.org/10.1017/jfm.2013.389>.
- [33] Aste T, Saadafar M, Sakellariou A, Senden TJ. Investigating the geometrical structure of disordered sphere packings. *Physica A Stat Mech* 2004;339(1–2):16–23. <http://dx.doi.org/10.1016/j.physa.2004.03.034>.
- [34] Bloom M, Russell M, Kustau A, Muriel K, Mandayam S. Measurement of granular material packing. *AIP Conf Proc* 2009;1145:195. <http://dx.doi.org/10.1063/1.3179890>.
- [35] Ribeiro M, Neto P, Pinho C. Mean porosity and pressure drop measurements in packed beds of monosized spheres: side wall effects. *Int Rev Chem Eng* 2010;2(1):40–6.